

Linear and Nonlinear Disturbance Evolution on the Frustum of Hypersonic Ogive-Cylinders

Hemanth Goparaju*

The Ohio State University, Columbus, Ohio, 43210

Kunal C. Kanawade†

Florida State University, Tallahassee, Florida, 32310

S. Unnikrishnan‡

Florida State University, Tallahassee, Florida, 32310

Datta V. Gaitonde§

The Ohio State University, Columbus, Ohio, 43210

Aspects of transition mechanisms on a 14° sharp-nosed ogive-cylinder at Mach 6 are elucidated by considering linear and nonlinear disturbance evolution of freestream stochastic and wave packet forcing at different locations downstream of the ogive-cylinder junction. The spectral response of the stochastic forcing displays favorable agreement with experimental observations from AFRL on which the configuration is based. Intermittent wave packets are generated from small-amplitude continuous freestream pressure forcing. Linear wave packet evolution reveals that Mack modes are the dominant primary instabilities, followed by relatively weaker first-mode waves. The non-linear wavepacket displays a three-legged wall pressure perturbation signature, which is traced to spanwise curvature effects, and fundamental resonance is the dominant secondary instability mechanism. At higher amplitudes of excitation, weak signatures of sub-harmonic and oblique resonance phenomena are identified. Downstream placement of the small-amplitude disturbance diminishes receptivity of first-mode waves; however, with high-amplitude forcing, the location of actuation does not significantly vary the disturbance evolution signature or the secondary instability mechanisms.

Nomenclature

M	=	Mach number
μ	=	dynamic viscosity coefficient
γ	=	specific heat ratio

*Graduate Research Assistant, Mechanical and Aerospace Engineering

†Graduate Research Assistant, Mechanical Engineering

‡Assistant Professor, Mechanical Engineering

§Glenn Chair Professor, Mechanical and Aerospace Engineering, AIAA Fellow

Pr	=	Prandtl number
Re	=	Reynolds number
f	=	frequency [kHz]
ω	=	angular frequency
(α, β)	=	streamwise, spanwise wavenumbers
λ_z	=	spanwise wavelength
δ_h	=	boundary-layer thickness
ϵ	=	amplitude parameter
r	=	random number
ρ	=	density
p	=	pressure
T	=	temperature
t	=	time coordinate
e	=	total energy
H	=	specific enthalpy
Q	=	vectors of conserved variables in body-fitted coordinates
(u, v, w)	=	streamwise, wall-normal, spanwise velocity components in Cartesian coordinates
(ξ, η, ζ)	=	streamwise, wall-normal, azimuthal coordinates in body-fitted coordinate system
(x, y, z)	=	streamwise, wall-normal, azimuthal coordinates in Cartesian coordinate system
(E, G, F)	=	flux vectors in (ξ, η, ζ) directions
J	=	transformation Jacobian matrix
τ	=	stress tensor
\bar{I}	=	heat flux
Subscripts		
∞	=	Freestream conditions
e	=	boundary-layer edge
w	=	wall conditions
n	=	wall -normal component
C	=	vectors in Cartesian coordinates
Superscript		
$'$	=	perturbation

I. Introduction

The location of laminar-turbulent transition in high-speed boundary layers is crucial in the design of hypersonic aircraft because of its influence on drag and wall heating. The development of accurate models to predict this location is a challenging endeavor because of the numerous possible transition paths, which depend on the nature of mean flow and freestream disturbances [1]. In wind tunnels, hypersonic transition experiments have mainly been performed on canonical configurations such as flat plates, wedges, and cones. A comprehensive documentation of studies until the beginning of the 21st century may be found in Schneider [2]. Numerous recent ground test experiments have greatly enriched the available databases. Mean flow variations have been incorporated by varying the leading edge bluntness, angle of attack, and surface roughness. Mean flow modifications due to ogive forebodies are known to result in improved drag and heating performance. Experimental and numerical studies characterizing transition in these configurations are, however, relatively scarce. The present work focuses on a numerical examination of transition mechanisms on the frustum of a sharp ogive cylinder. The configurational parameters are anchored in recent conventional (noisy) Air Force Research Laboratory Mach-6 Ludwig Tube experiments by Hill et al. [3], which are described in Sec. III.A.

Transition in convectively unstable boundary layers may be viewed as a forced response of a complex oscillator [4]. The boundary-layer essentially acts as an amplifier, with its transition depending on the nature and spectral content of freestream disturbances, and their selective amplification [5]. Freestream disturbances have low amplitudes in typical atmospheric flight scenarios, where transition to turbulence displays three main phases including, receptivity, linear disturbance amplification, and nonlinear modulation leading to turbulence. Receptivity is the process through which environmental fluctuations penetrate the boundary layer. In low-speed flows at zero angle of attack, the evolution of linear disturbances is described in terms of planar Tollmien-Schlichting waves [6]. With increasing flow speeds to the supersonic regime, the most amplified waves are oblique first modes.

At even higher speeds, in hypersonic flows, a direct resonance is observed between freestream acoustic waves and boundary layer modes [7] and the wavelength conversion mechanism of low-speed flows [8] is no longer needed. In sharp-nosed axisymmetric cones and flat plates, Mack [9] derived the existence of a family of higher instability modes (called Mack modes). At freestream Mach numbers higher than 4, the first of these, designated the second-mode, displayed growth rates exceeding those of the first mode [10]. The characterization of the second mode in terms of fast and slow acoustic waves and the F and S instability nomenclature has been discussed in detail by Fedorov and Tumin [11]. Under typical wind tunnel conditions, Kendall [12] established second-mode disturbances as the dominant primary instabilities for axisymmetric cones. More recently, Scholten et al. [13] used modal stability analyses, which do not account for receptivity, to identify Mack modes as the dominant primary instabilities for hypersonic sharp ogive cylinders. In the last stage of the transition, when amplitudes are sufficiently high, the primary instabilities saturate and transfer energy to other disturbances through triadic interactions [14]. These disturbances interact non-linearly, leading to spectral filling and turbulence.

During transition, the nature and composition of freestream perturbations set the initial conditions (frequency, phase, amplitude) that dictate subsequent disturbance evolution. In wind tunnels and free flight, perturbation sources include acoustic radiation from tunnel walls, entropic spots, vortical gusts, and particulates [15]. It is difficult to numerically specify the composition of these disturbances, as they remain largely unknown [2]. However, various more recent efforts have been made to model the broadband nature of the tunnel or free-flight disturbances. Balakumar and Chou [16] simulated freestream disturbances based on Mach 10 sharp cone experiments by Marineau et al. [17] to successfully predict the location of the onset of the transition. Reduced order models to inform the inlet disturbances can be developed if a high-fidelity tunnel simulation is available. For example, Goparaju et al. [18], Liu et al. [19] developed such models based on Duan et al. [20] turbulence data sets and captured first- and second-mode driven breakdown at Mach 2.5 and 8, respectively.

In the absence of relevant experimental or numerical wind tunnel data, freestream perturbations have been successfully modeled as stochastic perturbations following the work of Hader and Fasel [21], who used the approach to show that fundamental breakdown is the dominant route to turbulence in flared cones at Mach 6. Later, Goparaju et al. [22] used this perturbation specification approach to examine the role of leading edge bluntness in hypersonic flat plates. The evolution of linear disturbances highlighted a change in the nature of instability waves at higher nose radii. Since a detailed composition of freestream perturbations in the tunnels used by Hill et al. [3] is currently lacking, we use this stochastic approach to model inlet pressure perturbations in Sec. III.B.

The role of other sources of disturbances during transition described by Bushnell [15] has also been quantified in the literature. Fedorov et al. [23] modeled freestream entropy-spots to note the generation of instability mode F [11] inside the boundary layer, and downstream excitation of mode S (second mode in this case) through the intermodal exchange mechanism. Second-mode receptivity of slow freestream acoustic waves was shown to be stronger than that of fast acoustic waves on supersonic flat plates by Ma and Zhong [24]. Furthermore, freestream entropy and vorticity receptivity were very similar to those of freestream fast acoustic waves. On hypersonic cylinder-wedges, Cerminara and Sandham [25] showed strong resonant amplification of the F -mode closer to the leading edge with freestream fast acoustic forcing.

In addition to stochastic freestream excitation, we also consider wavepacket forcing, which has proven very insightful in isolating transition mechanisms in a controlled manner. The physical motivation for such excitation stems from the fact that solid particulate impact can excite instability waves in high speed boundary layers, as elucidated in the theoretical model of Fedorov [26]. Direct numerical simulations of Chuvakhov et al [27] demonstrate that particle interactions can indeed generate wave packets; this was shown to result in transition on a 14° half-angle wedge at Mach 4. Hader and Fasel [28] showed that the evolution of a localized pulse (wave packet) is a good surrogate to model particle impact effects. These results have led to the extensive use of wave packet analysis to simulate aspects of natural transition, i.e., through broadband disturbance initiation (see, [28, 29]). In tests, such pulses were generated

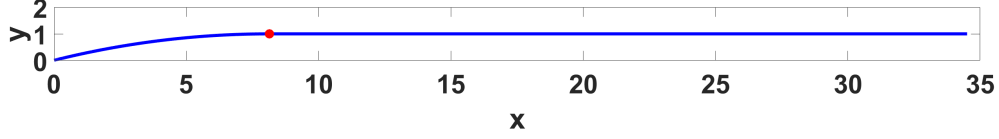


Fig. 1 Profile of the ogive-cylinder forebody with junction marked in red.

on hypersonic wind tunnel walls by Casper et al. [30] through glow discharges, and the evolution of disturbances was tracked from the linear to the breakdown stages.

The goal of the present work is to examine transition mechanisms on ogive cylinders, so as to complement analogous studies on cones [28, 29] and flat plates [31, 32]. The key consideration that distinguishes ogive cylinders from these configurations is the presence of significant spanwise curvature throughout the streamwise length. The linear and nonlinear stages of transition in these geometries are addressed in Sec. III.C through wave packet analysis.

This paper is organized as follows. The geometry and numerical methods are discussed in Sec. II. Steady base flow features, followed by linear and nonlinear disturbance evolution, are examined in Sec. III. The conclusions of this work are provided in Sec. IV.

II. Flow Configuration and Numerical Methodology

The forebody geometry and the freestream parameters are first described, followed by a description of the numerical methods and procedures used.

A. Geometry

The forebody mimics the Mach 6 experiments of Hill et al. [3] and is comprised of an ogive cylinder of half-angle 14° and nose radius $0.1mm$, which is considered to be sharp. The forebody length is $0.253m$ beyond which it is tangentially joined to a cylinder of radius $0.0311m$, and length $1m$. Lengths are non-dimensionalized by the cylinder radius; the body profile in terms of the streamwise (x) and wall-normal (y) directions is shown in Fig. 1. The ogive-cylinder junction is thus located at $x=8.135$ (marked in the figure) and the cylinder section extends until the end of the domain.

The freestream parameters are based on the Mach 6 Ludwig Tube wind tunnel conditions at the Air Force Research Laboratory (AFRL). The angle of attack is specified to be zero, and the freestream Mach number is 6.1. The oncoming flow is at a Reynolds number $Re = 7.01 \times 10^6/m$. The temperature of the freestream (T_∞) is $58.01K$, and the wall is isothermal, (T_w) at $300K$. This results in a slightly cooled wall relative to the recovery temperature for these freestream conditions.

B. Numerical Techniques and Boundary Conditions

The flow is modeled using unsteady viscous compressible Navier-Stokes equations, cast in the strong conservative form as:

$$\frac{\partial \mathbf{Q}}{\partial t} + \frac{\partial \mathbf{E}}{\partial \xi} + \frac{\partial \mathbf{G}}{\partial \eta} + \frac{\partial \mathbf{F}}{\partial \zeta} = 0 \quad (1)$$

where t is the time and (ξ, η, ζ) are the spatial coordinates. \mathbf{Q} is the vector of conservative variables, and $(\mathbf{E}, \mathbf{G}, \mathbf{F})$ are flux vectors that satisfy the relation:

$$\begin{aligned} \mathbf{Q} &= J \mathbf{Q}_c, \quad \mathbf{E} = J \left(\mathbf{E}_c \frac{\partial \xi}{\partial x} + \mathbf{G}_c \frac{\partial \xi}{\partial y} + \mathbf{F}_c \frac{\partial \xi}{\partial z} \right) \\ \mathbf{G} &= J \left(\mathbf{E}_c \frac{\partial \eta}{\partial x} + \mathbf{G}_c \frac{\partial \eta}{\partial y} + \mathbf{F}_c \frac{\partial \eta}{\partial z} \right), \\ \mathbf{F} &= J \left(\mathbf{E}_c \frac{\partial \zeta}{\partial x} + \mathbf{G}_c \frac{\partial \zeta}{\partial y} + \mathbf{F}_c \frac{\partial \zeta}{\partial z} \right) \end{aligned} \quad (2)$$

Here, $\mathbf{J} = \det[\partial(x, y, z)/\partial(\xi, \eta, \zeta)]$ is the Jacobian of the coordinate transformation and $(\mathbf{E}_c, \mathbf{G}_c, \mathbf{F}_c)$ are given by:

$$\mathbf{Q}_c = \begin{bmatrix} \rho \\ \rho u \\ \rho v \\ \rho w \\ \rho e \end{bmatrix}, \quad \mathbf{E}_c = \begin{bmatrix} \rho u \\ \rho u u + p + \tau_{xx}/Re_\infty \\ \rho u v + \tau_{xy}/Re_\infty \\ \rho u w + \tau_{xz}/Re_\infty \\ \rho u H + I_x/Re_\infty \end{bmatrix}, \quad \mathbf{G}_c = \begin{bmatrix} \rho v \\ \rho v u + \tau_{yx}/Re_\infty \\ \rho v v + p + \tau_{yy}/Re_\infty \\ \rho v w + \tau_{yz}/Re_\infty \\ \rho v H + I_y/Re_\infty \end{bmatrix}, \quad \mathbf{F}_c = \begin{bmatrix} \rho w \\ \rho w u + \tau_{zx}/Re_\infty \\ \rho w v + \tau_{zy}/Re_\infty \\ \rho w w + p + \tau_{zz}/Re_\infty \\ \rho w H + I_z/Re_\infty \end{bmatrix} \quad (3)$$

The total energy per unit volume (e) and the total specific enthalpy (H) are obtained from:

$$\begin{aligned} e &= \frac{p}{\rho(\gamma - 1)} + \frac{1}{2} (u^2 + v^2 + w^2), \\ H &= \frac{T}{\gamma - 1 M_\infty^2} + \frac{1}{2} (u^2 + v^2 + w^2) \end{aligned} \quad (4)$$

The components of stress tensor (τ) are:

$$\begin{aligned} \tau_{xx} &= -\mu \left(2 \frac{\partial u}{\partial x} - \frac{2}{3} \text{div } V \right), \quad \tau_{yy} = -\mu \left(2 \frac{\partial v}{\partial y} - \frac{2}{3} \text{div } V \right) \\ \tau_{zz} &= -\mu \left(2 \frac{\partial w}{\partial z} - \frac{2}{3} \text{div } V \right) \\ \tau_{xy} &= -\mu \left(\frac{\partial u}{\partial y} + \frac{\partial v}{\partial x} \right), \quad \tau_{xz} = -\mu \left(\frac{\partial u}{\partial z} + \frac{\partial w}{\partial x} \right) \\ \tau_{yz} &= -\mu \left(\frac{\partial v}{\partial z} + \frac{\partial w}{\partial y} \right) \end{aligned} \quad (5)$$

The heat flux vector components are:

$$\begin{aligned}
I_x &= (u\tau_{xx} + v\tau_{xy} + w\tau_{xz}) - \lambda \frac{\partial T}{\partial x} \\
I_y &= (u\tau_{yx} + v\tau_{yy} + w\tau_{yz}) - \lambda \frac{\partial T}{\partial y} \\
I_z &= (u\tau_{zx} + v\tau_{zy} + w\tau_{zz}) - \lambda \frac{\partial T}{\partial z} \\
\lambda &= \frac{\mu}{\text{Pr}(\gamma - 1)M_\infty^2}
\end{aligned} \tag{6}$$

The equation of state closes the equations:

$$p = \frac{\rho T}{\gamma M_\infty^2} \tag{7}$$

As noted earlier length-scales are normalized by the radius of cylindrical section ($l = 0.0311 \text{ m}$). Velocity, density, and temperature are normalized by the corresponding freestream quantities, while pressure is normalized by twice the freestream dynamic pressure ($\rho_\infty u_\infty^2$). Unless specified otherwise, all quantities are reported in nondimensional form. The working gas is assumed to be calorically perfect with Prandtl number ($Pr = 0.72$), and ratio of specific heat $\gamma = 1.4$. Viscosity is calculated using Sutherland's law, $\mu = T^{3/2}(S + 1)/(S + T)$, where $S = 110/T_\infty$, and the second viscosity is modeled by the Stokes hypothesis.

The unsteady 3D simulations are predicated on precursor base flow simulations that include the leading edge of the geometry are performed using an axisymmetric solver formulated in the generalized cylindrical coordinates[33]. The grid has $3,251 \times 601$ points in the streamwise (x) and wall-normal (y) directions, respectively. 50% of wall-normal points are clustered in the boundary-layer, and in the streamwise extent, the wave corresponding to largest frequency is resolved by 40 points. These are comparable to earlier transitional numerical simulations (see, *e.g.*, Ref. [5]). Since the precursor calculations are designed primarily to capture the laminar basic state and shock, second-order accurate schemes are used for the convective and viscous fluxes with artificial dissipation for numerical stability[34]. Symmetry conditions are imposed along the axis upstream of the nose, Dirichlet boundary conditions are imposed on the freestream boundary, the wall is treated as a no-slip isothermal boundary with $T_w/T_\infty = 5.16$, and a zero-gradient condition is applied on the downstream outflow boundary.

After the convergence of the axisymmetric base flow, the domain downstream of the ogive-cylinder junction is extracted from $x = 9.0$, and rotated in the azimuthal direction within the range $\theta \in [-90^\circ, 90^\circ]$ for three-dimensional calculations using 225 azimuthal points. The base flow is reconverged in time with the higher-order numerical scheme described below to serve as the basic state for perturbation evolution. Time-marching is performed using the second-order implicit Beam and Warming technique [35]. Inviscid fluxes are reconstructed with the seventh-order WENO scheme [36], and solved with the Roe-Riemann solver [37]. Viscous fluxes are evaluated through sixth-order compact-like schemes [38]. At the inlet, the first five streamwise points from the 2D computations are extracted from

Table 1 Simulation cases considered in this work

Case	Forcing Nature	Forcing Location	Amplitude
1	Stochastic forcing- 2D	$x = 9.0$	Linear
2	Stochastic forcing- 3D	$x = 9.0$	Linear
3	Wave packet- 3D	$x = 9.46$	Linear
4	Wave packet- 3D	$x = 16.2$	Linear
5	Wave packet- 3D	$x = 9.46$	Nonlinear
6	Wave packet- 3D	$x = 16.2$	Nonlinear

the wall-normal data. These values are converted to cylindrical coordinates and imposed on the azimuthal plane as Dirichlet boundary conditions for the 3D computations. The wall and freestream boundary conditions remain the same. At the azimuthal boundaries i.e., the azimuthal velocity (v_θ) is antisymmetric while the radial velocity (v_r) is symmetric. Zero-gradient conditions are imposed at the exit of the domain.

C. Disturbance Generation

The characteristics of disturbance evolution on the converged base flows are examined separately with stochastic and wave packet forcing. For stochastic forcing, pressure perturbations (p') are specified on the inlet plane:

$$\frac{p'}{\rho_\infty u_\infty^2} = \epsilon(2r - 1), \quad (8)$$

where ϵ is the amplitude of the forcing. Random numbers $r \in [0, 1]$ are generated with an inbuilt FORTRAN function following the work of Hader and Fasel [21]. This generates spatio-temporally varying disturbances at the inlet plane. For two-dimensional studies, this forcing results in the evolution of axisymmetric disturbances while for the three-dimensional cases, the forcing has a delta form in the azimuthal direction, generating spanwise gradients.

Wavepacket forcing imposes localized pulses with a forcing function centered around the frequency ω :

$$q_w(x, z, t) = (\rho v_n)_w = \epsilon \sin^3 \left(2\pi \frac{x - x_1}{x_2 - x_1} \right) \sin^3 \left(\pi \frac{z - z_1}{z_2 - z_1} \right) \sin(\omega t), \quad (9)$$

$$x_1 \leq x \leq x_2, \quad z_1 \leq z \leq z_2, \quad 0 \leq t \leq t_1$$

The wall-normal momentum is excited, ensuring smooth gradients at the actuator edges, by blowing-suction in the streamwise extent $x \in [x_1, x_2]$ as a dipole of width 0.02. In unrolled azimuthal coordinates, the slot $z \in [z_1, z_2]$ is excited by a monopole forcing function with width 0.01. A wave packet at frequency ω is triggered in $t \in [0, t_1]$, with $t_1 = 2\pi/\omega$. The amplitude ϵ can be varied to generate waves of different strengths. Various cases are examined in this work, encompassing linear and nonlinear receptivity and disturbance evolution, and are summarized in Table 1.

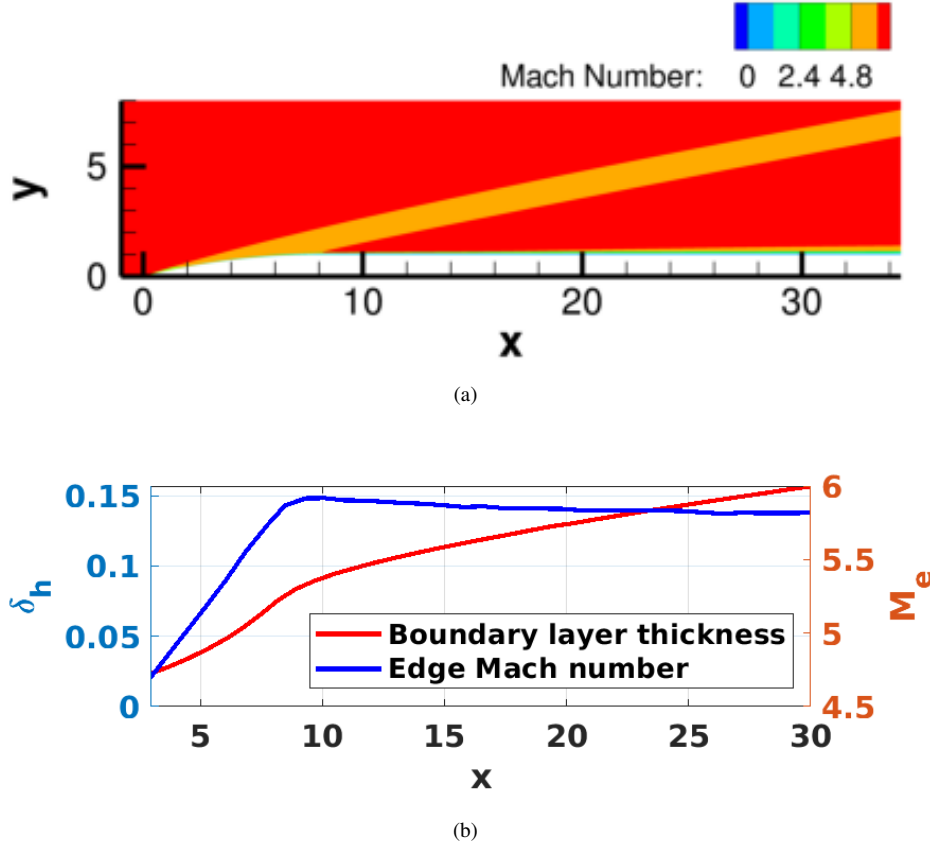


Fig. 2 Steady base flow features of ogive-cylinder depicting (a) Mach number contours (b) Boundary layer edge properties.

III. Results

A. Steady Base Flow

An accurate prediction of the steady base flow is vital for the study of small-amplitude perturbation evolution [5]. The steady base flow features for the ogive cylinder are shown in Fig. 2. The Mach number contours in Fig. 2(a) show the shock structure. The detached shock region is associated with the relatively small ogive nose radius; it subsequently curves because of favorable pressure gradients arising from the curved ogive portion, and ultimately weakens to a Mach wave at the exit of the domain. A comparison of velocity and entropy profiles revealed that no significant entropy gradients exist outside the boundary layer, due to the relatively small shock curvature radius on the ogive portion.

The edge of the boundary layer (δ_h) is chosen as the wall normal distance where the ratio of total enthalpy to the freestream enthalpy reaches 0.995 [39]. The streamwise evolution of δ_h , shown in Fig. 2(b), indicates a monotonic increase with a change in growth rate evident at the junction of the ogive with the cylinder. The boundary layer edge Mach number (M_e), considered at a wall normal height $1.5\delta_h$, is also shown in Fig. 2(b). The value of about $M_e \sim 6.0$ over the length of the cylinder provides a preliminary indication of the potential dominance of the Mack (or second)

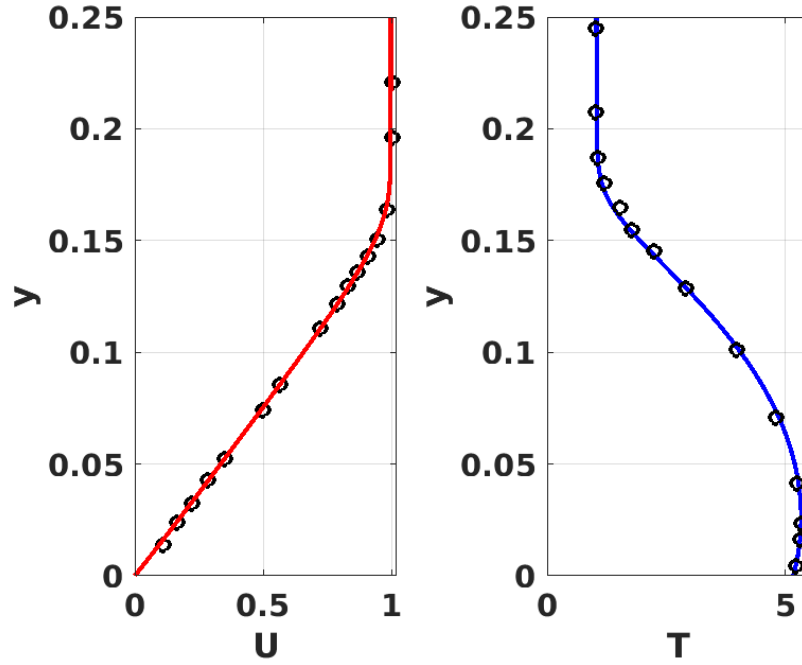


Fig. 3 Wall-normal base flow profiles at $x = 27.4$ for streamwise velocity (U) and temperature (T). The black circles (\circ) denote the profiles extracted from Scholten et al. [13].

mode.

The wall-normal streamwise velocity (U) and temperature (T) profiles extracted near the end of the domain ($x = 27$) or equivalently $0.6m$ from the junction of the ogive-cylinder are shown in Fig. 3. A good match with the corresponding profiles extracted from Scholten et al. [13] validates the accuracy of the current base flow.

B. Stochastic Linear Disturbance Evolution

1. Two-dimensional Perturbation Evolution

The response of the axisymmetric boundary layer to stochastic forcing from the freestream is first examined to characterize linear disturbance amplification, for which a small amplitude of $\epsilon = 1 \times 10^{-4}$ (Case 1) is used. The power spectral density of the wall pressure perturbations versus the streamwise distance is displayed in Figure 4. The most amplified disturbances lie in the relatively high-frequency range ($f \in [60 - 120kHz]$), and scale inversely with the thickness of the boundary layer, which are consistent with the properties of second mode instability [17].

The streamwise amplification of the disturbances is further quantified by the N-factor, defined as the logarithm of the ratio of the amplitude of a perturbation quantity at a given x location to its amplitude at a reference location, x_0 . Here, the reference location is chosen as that where the linear growth in log scale is initiated in wall pressure perturbation data. The N-factor curves, shown in Fig. 5, indicate that higher frequencies are more amplified closer to the actuation location i.e., the lower frequencies indicate peaks at larger streamwise distances. These curves are consistent with the

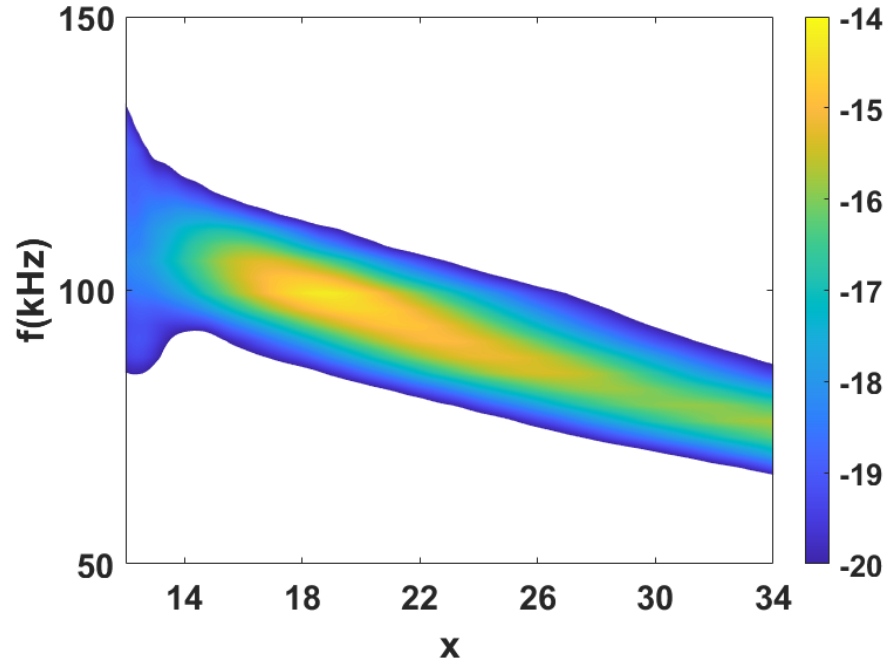


Fig. 4 Frequency(f)- streamwise (x) contours depicting the power spectral density of wall pressure perturbations with 2D stochastic forcing (Case 1).

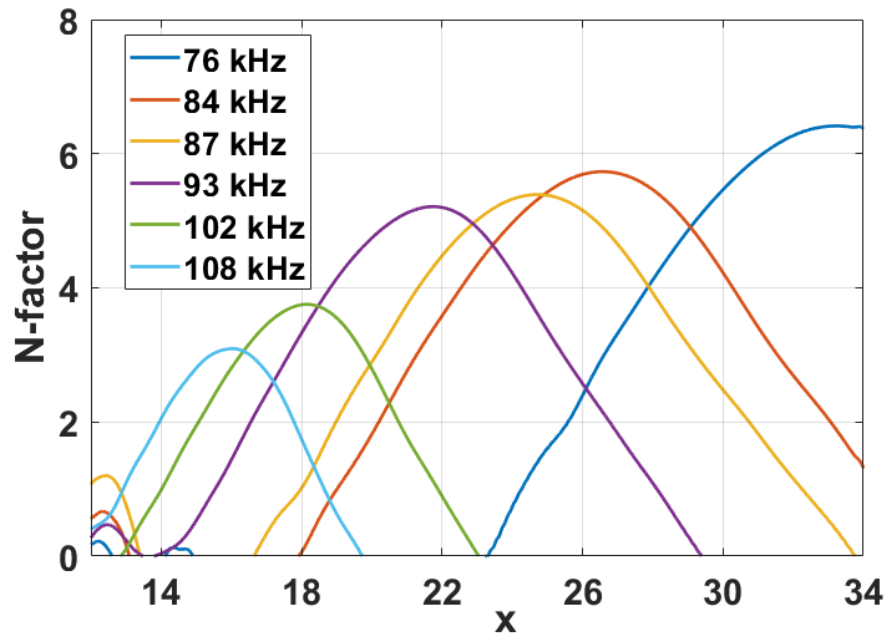


Fig. 5 N-factor curves from wall pressure perturbations comparing relative amplification, obtained from 2D stochastic forcing (Case 1).

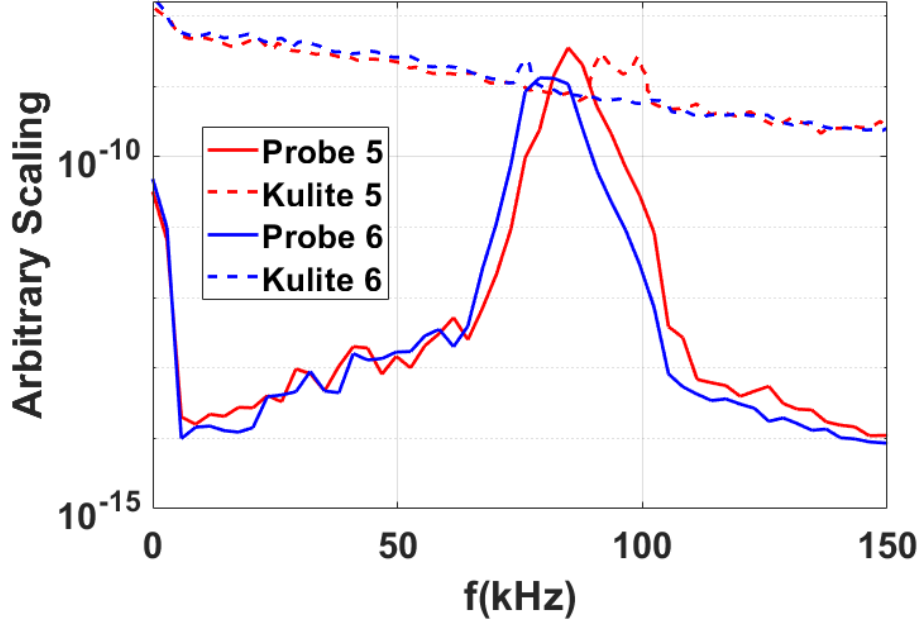


Fig. 6 Comparison of experimental and numerical wall pressure spectral data (Case 1). The Kulite data is extracted from Hill et al. [3].

modal instability analysis performed by Scholten et al. [40]. The streamwise extent of the disturbance amplification zone increases with decreasing frequencies.

The response to stochastic forcing is validated with the pressure transducer probes of Hill et al. [3] in Fig. 6. The experimental measurements (dashed lines) and the corresponding computational probe measurements (solid lines) are compared for Kulites designated #5 and #6, located at $x = 26.7$ and 29.6 respectively, in the computational domain. The peak amplification at these two locations correspond to $f \sim 85$ and 75 kHz , respectively, which is in good agreement with the experimental observations. This confirms that the numerical technique, including the chosen stochastic forcing, effectively captures the most amplified waves.

2. Three-dimensional Perturbation Evolution

The three-dimensional response of the ogive cylinder boundary layer to broadband stochastic pressure fluctuations is examined using Case 2. To ensure linearity, an amplitude of $\epsilon = 1 \times 10^{-3}$ is used. Flow statistics are collected after the initial transients exit the domain. The temporal features of the wall pressure perturbation at a typical streamwise location ($x = 25$) are shown in Fig. 7. The disturbance signature (Fig. 7(a), top) is modulated in amplitude, indicating that despite the stochastic nature of the input, the perturbations organize and travel in groups as packets. This behavior is consistent with experimental [41] and numerical stochastic transition studies [21].

The wall pressure signal is filtered into frequency bands based on the response shown earlier in Fig. 4 of the 2D stochastic analysis. The signal extracted in the range $f \in [60 - 150 \text{ kHz}]$ in Fig. 7(a) (middle) exhibits similar structure

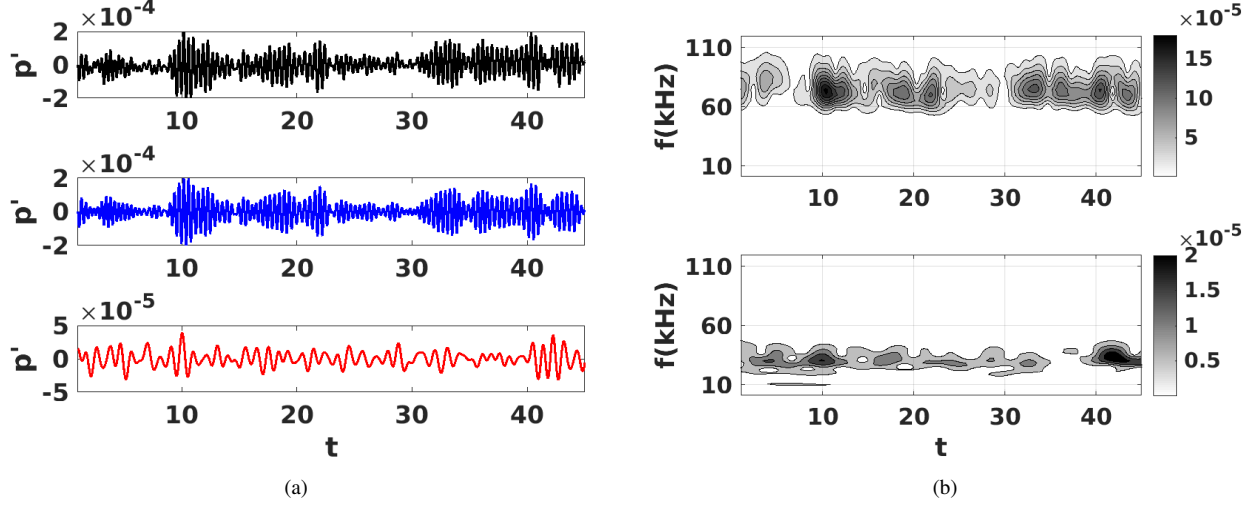


Fig. 7 Features of wall pressure perturbation probe at $x = 25$ (Case 2). In (a) raw signal (top), bandpass signals $[60 - 150 \text{ kHz}]$ (middle), $[10 - 40 \text{ kHz}]$ (bottom) are shown. In (b) scalogram of high (top) and low (bottom) bandpass signals are depicted.

as the original signal but with further amplitude modulation. The corresponding frequency evolution (scalogram) in Fig. 7(b) (top) attributes this to intermittent wave packets following each other. These waves have a relatively broad spectral content in the second mode (frequency) range with higher amplitudes in the local (maximum) Mack mode wave at $f \sim 70 \text{ kHz}$. The lower frequency content of the pressure signal extracted in the range $f \in [10 - 40 \text{ kHz}]$ (Fig. 7(a), bottom) displays weaker amplitudes. These disturbances have the characteristics of oblique first-mode waves, as they are not observed in Case 1. The corresponding scalogram (Fig. 7(b), bottom) also shows the wave intermittency behavior with amplification around $f \sim 30 \text{ kHz}$.

The evolution of disturbances is further characterized by identifying amplifying structures from the unsteady flow field. Since structures at specific frequencies are desired, an optimal data-driven choice is the dynamic mode decomposition (DMD) algorithm of Schmid [42]. The information obtained with this approach is similar to the Fourier transformation, where DMD provides a best-fit linear approximation with fewer snapshots [43]. Flow snapshots corresponding to the disturbance field, extracted by subtracting the mean of the snapshots, are processed for both wall and symmetry planes.

The frequency-amplitude distribution of the pressure perturbation field is shown in Fig. 8. The values represent the relative amplification of disturbances in the considered domain and have been extracted with the DMD method which provides a best-fit result in the least-square sense. 1,000 snapshots separated by $\Delta t = 0.05$ are employed to provide a converged result. Fluctuations in two frequency ranges, $f \in [10 - 50 \text{ kHz}]$ and $f \in [60 - 100 \text{ kHz}]$, are highlighted. Based on the numerical neutral curve of Fig. 4, the latter corresponds to second-mode waves, while the former represents first-mode waves as discussed further below. The most amplified second mode wave ($f = 68.3 \text{ kHz}$) has an order of magnitude higher amplitude than the corresponding first-mode wave ($f = 28.5 \text{ kHz}$), reinforcing the

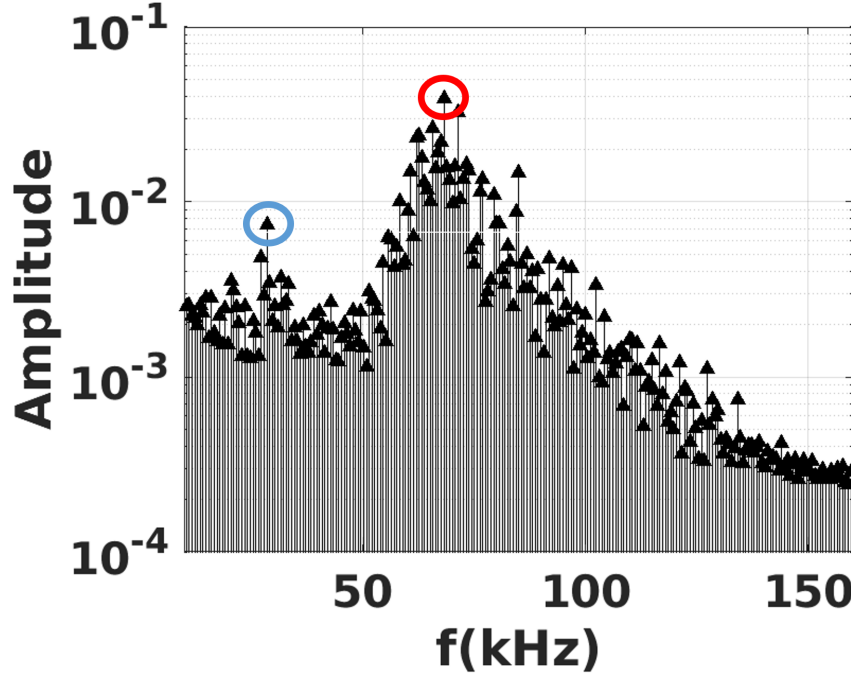
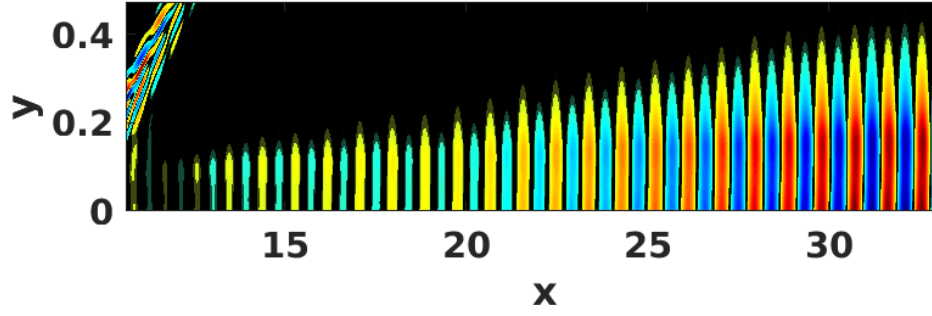


Fig. 8 Frequency-amplitude distribution for linear 3D stochastic forcing extracted from DMD analysis (Case 2).

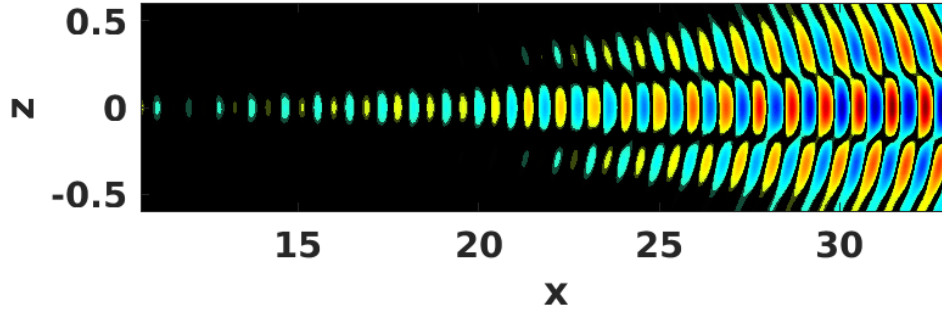
dominance of Mack modes in linear disturbance evolution on frustums of ogive-cylinders.

The characteristics of the modal structure at $f = 28.5 \text{ kHz}$ are shown in Fig. 9, with contour plots saturated to 80% of their maximum values for ease of interpretation. The pressure perturbation field (Fig. 9(a)) shows single lobe structures in the wall normal direction. The wall plane data, Fig. 9(b), are displayed by unrolling the spanwise cylinder surfaces with the relation $z = r\phi$, where r is the local radius of the cylinder (nondimensional) and ϕ is the azimuthal angle. In this plane, the structures are oblique confirming their first mode nature. The evolution of the pressure perturbation on the wall at $z = 0$ (Fig. 9(c)) shows wave amplification in the domain considered. Other disturbances in the frequency range $f \in [10 - 50 \text{ kHz}]$ also exhibit similar structures and hence can be classified as first-mode waves (see Mack [9]).

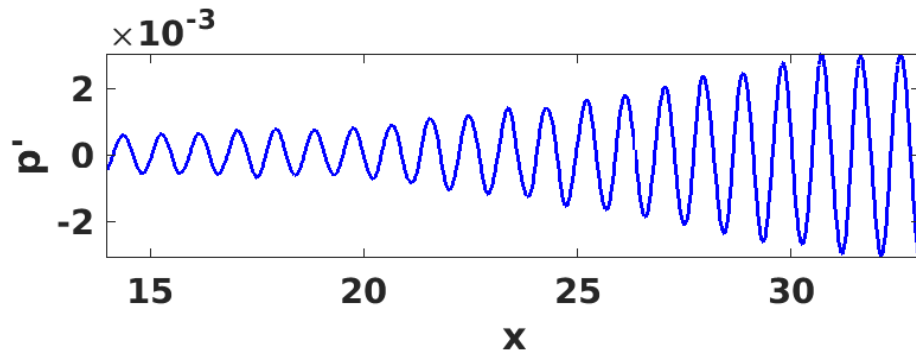
The disturbance characteristics of the most amplified wave at $f = 68.3 \text{ kHz}$ are depicted in Fig. 10. Unlike at the lower frequency, in this case, two-lobed structures are evident in the wall normal plane (Fig. 10(a)); these are indicative of Mack modes [9] and their spanwise signature (Fig. 10(b)) is predominantly two-dimensional. The amplification of these disturbances at the centerline in Fig. 10(c) shows relatively larger amplification over a smaller streamwise length than the first-mode wave shown earlier in Fig. 9(c). Other frequencies in $f \in [60 - 100 \text{ kHz}]$ exhibit similar structures; consistent with the N-factor figure presented earlier, amplitudes of higher frequencies peak at more upstream locations. A comparison of Figs. 9 and 10 indicates that first-mode waves have longer streamwise wavelengths than the second modes. While the former amplify over a longer streamwise extent, the latter exhibit larger amplification over a relatively smaller domain.



(a)

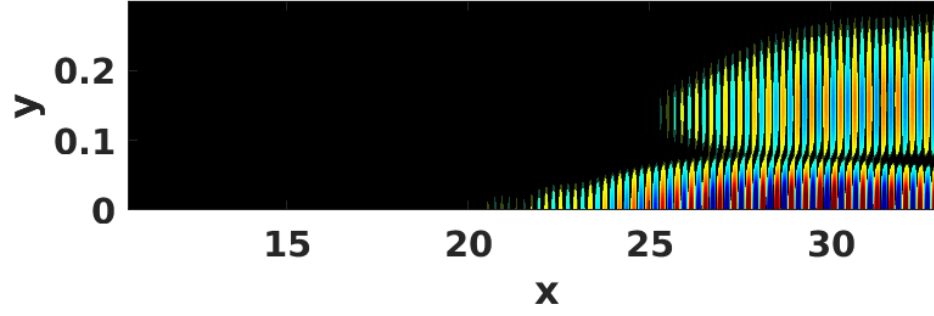


(b)

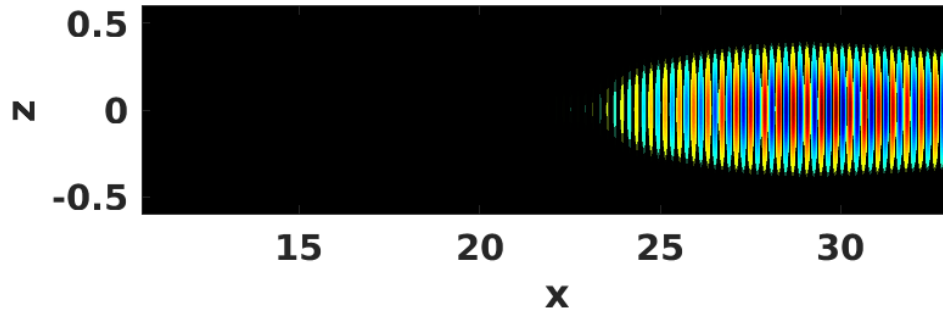


(c)

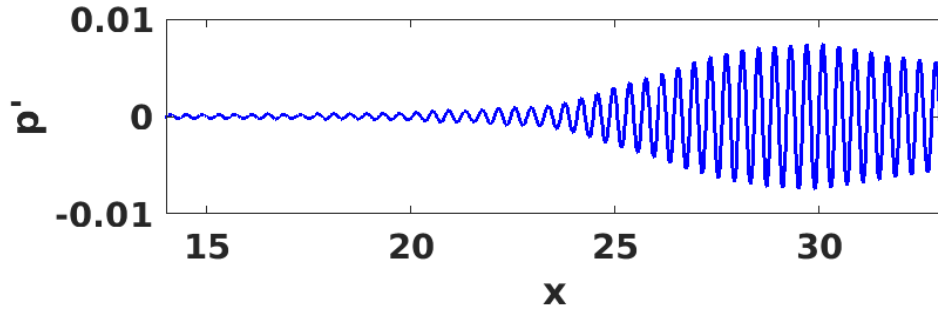
Fig. 9 DMD pressure mode features of first mode at $f = 28.55 kHz$. (a) Wall-normal signature at $z = 0$. (b) Spanwise signature at $y = 0$. (c) Amplitude evolution on the line $(y, z) = (0, 0)$.



(a)



(b)



(c)

Fig. 10 DMD pressure mode features of second mode at $f = 68.3kHz$. (a) Wall-normal signature at $z = 0$. (b) Spanwise signature at $y = 0$. (c) Amplitude evolution on the line $(y, z) = (0, 0)$.

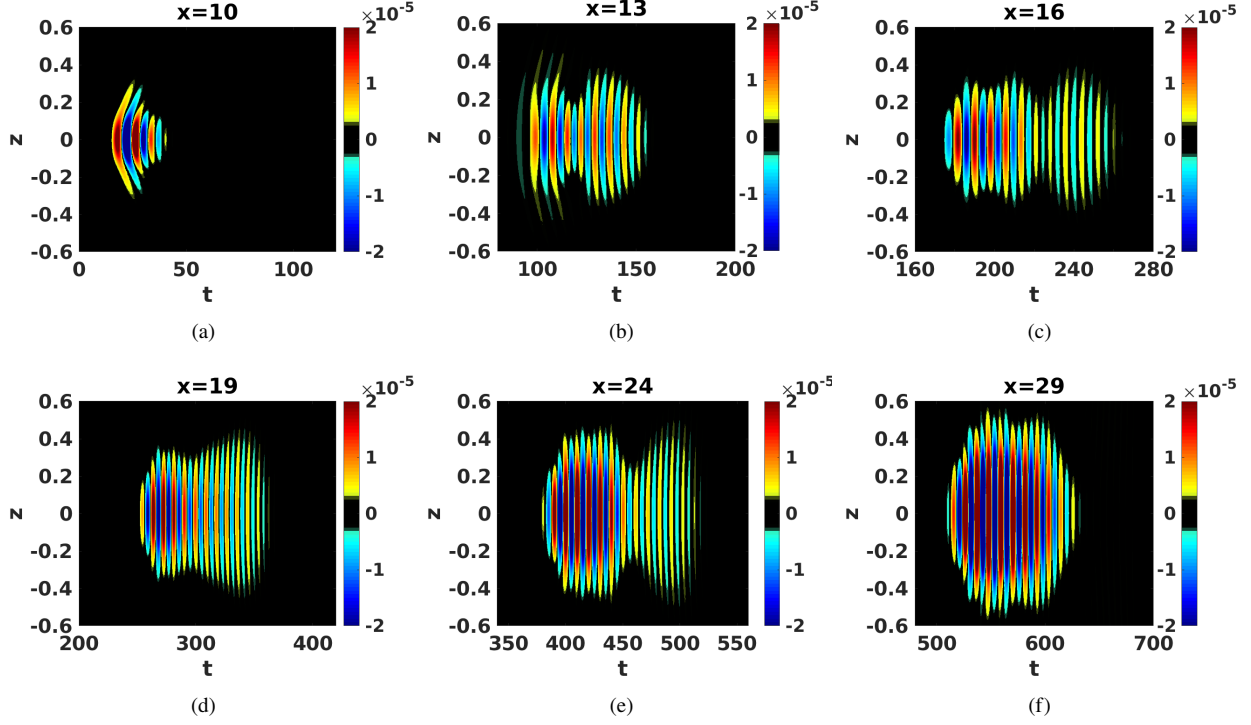


Fig. 11 Spatiotemporal evolution of wall pressure perturbations for linear wave packet forcing (Case 3).

C. Propagation of Three-dimensional Wave Packets

1. Linear Disturbance Evolution

To examine the three-dimensional features of linear disturbance amplification, a small-amplitude wave packet ($\epsilon = 5 \times 10^{-4}$) centered at $x = 9.46$ (Case 3) is triggered on the wall. This location is relatively closer to the ogive-cylinder junction, to exploit the fact that the natural receptivity is higher in this region. Figure 11 illustrates the spatiotemporal evolution of the wave packet disturbance (instantaneous minus steady laminar basic state) through the wall pressure perturbation signature at various streamwise locations. Since the horizontal axis represents non-dimensional time, the leftmost point on the contour corresponds to the signature of the leading edge of the wavepacket at the indicated streamwise location.

Initially, disturbances emanating from the forcing area ($x = 10$, Fig. 11(a)) have leading circular arc-like wave fronts. As the disturbances evolve ($x = 13$, Fig. 11(b)) however, arrowhead shaped structures develop behind these wave fronts. Further downstream ($x = 16$, Fig. 11(c)), the wave packet elongates in the streamwise axis and modulates in the spanwise extent. This structure resembles a flat plate wave packet, with oblique disturbances spread at the trailing edge [44]; on cones, the body curvature results in the formation of oblique waves at the center of the wave packet [45]. In the present case, the wave packet also develops through spreading at the trailing edge in the streamwise and azimuthal extents, as seen in $x = 19$ in Fig. 11(d). The relative amplitudes of the disturbances are higher in the leading arrowhead

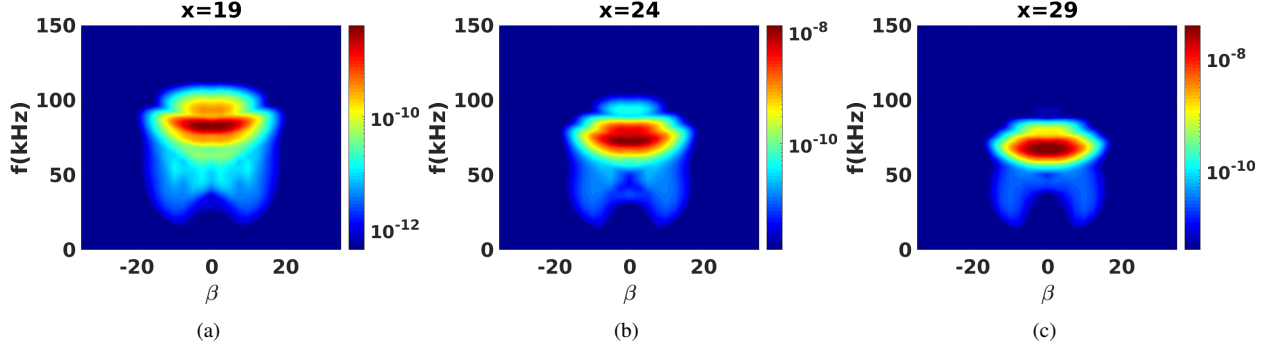


Fig. 12 Streamwise spectral evolution contours of the linear wave packet in the frequency (f)-spanwise wavenumber (β) plane (Case 3).

portion relative to the trailing waves, which is especially evident in Figs. 11(e,f) ($x = 24, 26$). Furthermore, they spread more in the streamwise rather than in the azimuthal direction.

Two-dimensional spanwise wavenumber-frequency ($\beta - f$) spectra of these disturbances, extracted by applying 2D Fourier transformation on the unrolled spanwise coordinates, are shown in Fig. 12. The spectral signature at $x = 19$ in Fig. 12(a) shows that two-dimensional ($\beta = 0$) high-frequency disturbances ($f \sim 82 \text{ kHz}$) have larger amplitudes than their oblique low-frequency ($f \sim 22 \text{ kHz}$) counterparts. The higher and lower amplitude waves correspond to the leading 2D Mack modes and the trailing first modes, respectively. The peak 2D frequency decreases downstream (Fig. 12(b,c)) ($f \sim 70.5 \text{ kHz}, 65.2 \text{ kHz}$, respectively), consistent with the inverse scaling of Mack modes with the thickness of the boundary layer [46]. The signature of the leading-wave amplification in Fig. 11(e,f) is also apparent in Fig. 12(b,c). Therefore, Mack modes dominate linear instabilities in this configuration, consistent with the stability analysis-based observations of Scholten et al. [13].

The effect of actuator location on instability evolution is examined by considering excitation at a downstream location of $x = 16.2$ (Case 4). The wall pressure perturbation signature along with its $\beta - f$ spectral distribution are shown in Fig. 13. At $x = 19$, Fig. 13(a), the wave packet displays an arrowhead shape with a predominantly 2D signature based on the wavenumber content of Fig. 13(d). These arrowhead structures develop further downstream (Fig. 13(b,c)) with no apparent signature of the trailing waves observed at the upstream actuator location (Fig. 11). The corresponding spectral distribution (Fig. 13(e,f)) captures Mack modes with decreasing frequency ($f \sim 70.5 \text{ kHz}, 65.2 \text{ kHz}$, respectively) and increasing amplitudes, similar to those in Fig. 12. However, the oblique wave signature is not observed in the Fourier plane.

The above wave packet analyses suggest that disturbance evolution depends on the location of actuation. In free flight, one possible source of such actuation may be particle impacts at different locations on the surface of the vehicle, with amplitude disturbance depending on the size of the particle [47]. Similar changes in receptivity have previously been observed using wave packets on sharp cones [28], compression corners [5], and blunted flat plates [48, 49]. On

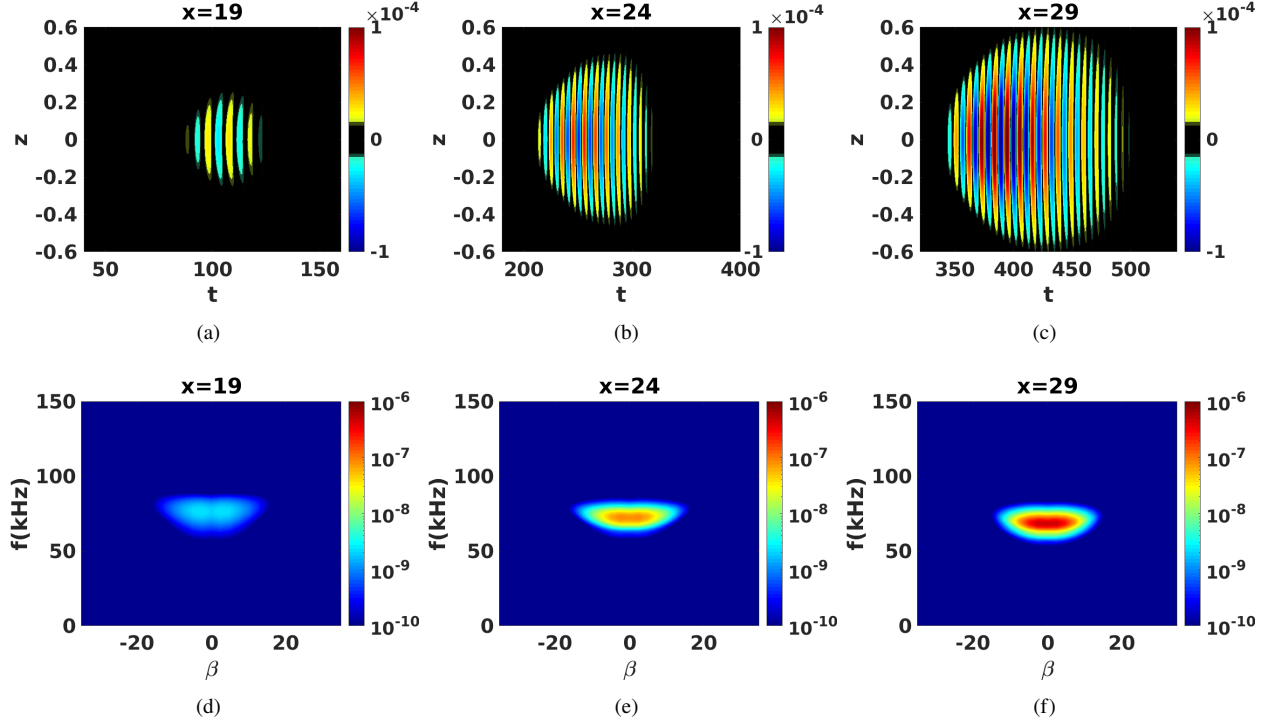


Fig. 13 Linear wave packet evolution for disturbances triggered at $x = 16.2$ (Case 4). Wall pressure perturbation contours are shown in (a, b, c) while the The corresponding spectral content is plotted in (d, e, f).

hypersonic sharp flat plates, Sivasubramanian et al. [31] attributed the differences in receptivity to the difference in flow sensitivity to the first and second discrete modes at different actuator locations.

The vortical structures manifested by Case 3 wave packet excitation are examined with Q -criterion [50] isosurfaces closer to the exit of the domain in Fig. 14. Two-dimensional roller-like structures typical of Mack modes are observed; consistent with wall pressure perturbation patterns, the oblique first-mode signature is not apparent. The wall-normal density gradient structures (pseudo-Schlieren) of this wave packet (at $z = 0$) shown in Fig. 15 exhibits *rope-like* structures. The maximum density gradient appears at the boundary-layer GIP (generalized inflection point [51]) at $y \sim 0.124$, with a nondimensional streamwise wavelength 0.5, resulting in a phase speed of 0.836. This is typical of Mack modes and was also reported by the experiments of Hill et al. [3]. The density perturbation field in the cross-flow plane at $x = 31$ (Fig. 16) shows structures near the wall $(y, z) \sim (0, 0)$, and at the edge of the boundary layer $(y, z) \sim (0.2, 0)$. The rope-like structures in the (experimental) Schlieren are manifestations of these stronger density perturbations, occurring away from the wall. Oblique waves with weaker amplitudes are also observed here with $\lambda_z \sim 0.62$ and correspond to those in Fig. 12(c).

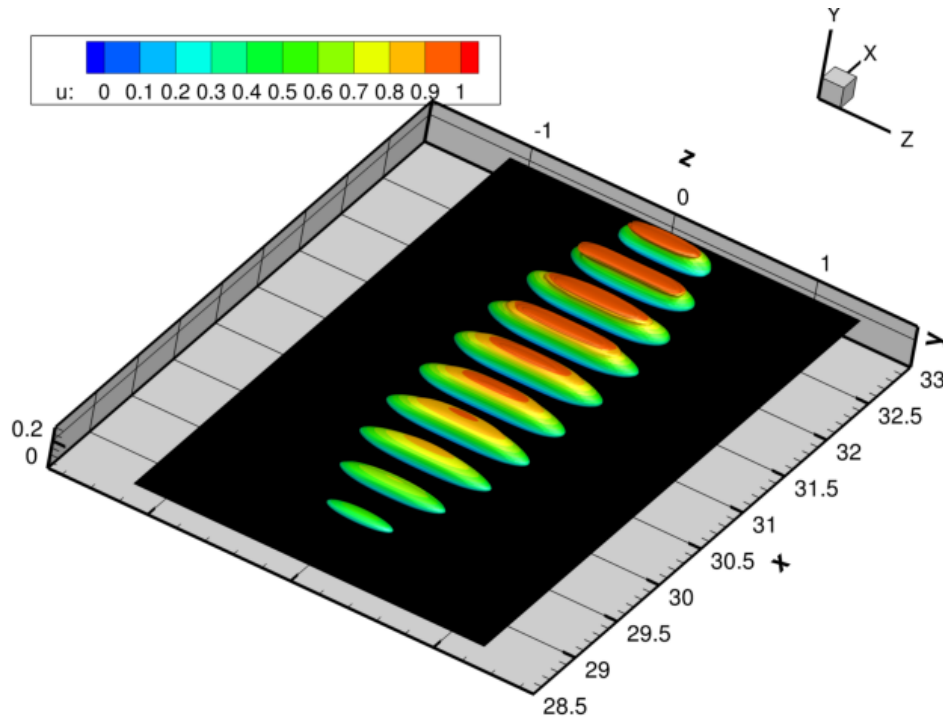


Fig. 14 Instantaneous vortical structures identified by the Q -criterion ($Q = 0.01$) isosurfaces extracted at the end of the domain for Case 3.

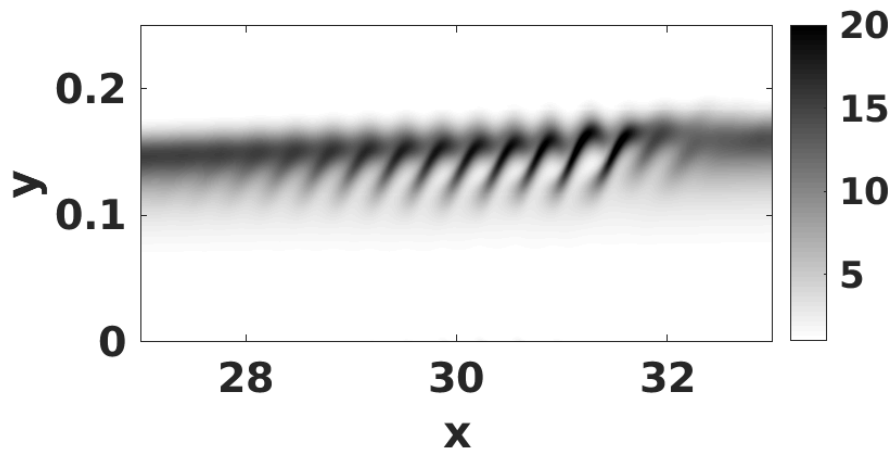


Fig. 15 Pseudo-Schlieren at the symmetry plane of the instantaneous vortical structures in Case 3.

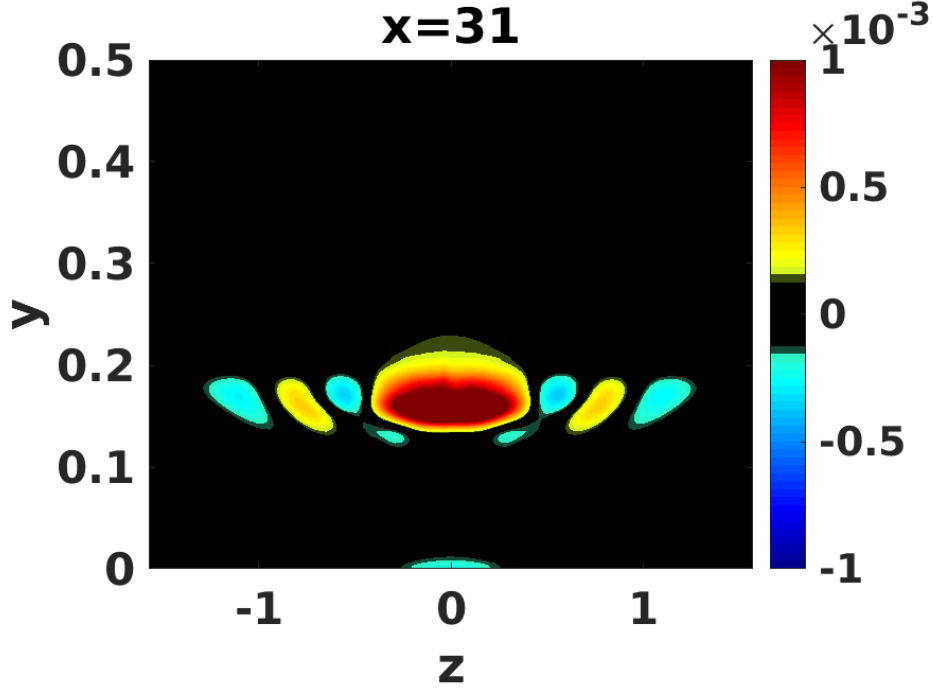


Fig. 16 Density perturbation contours in the cross-flow plane of instantaneous vortical structures (Case 3).

2. Nonlinear Modulation of Wave Packet

To examine the effects of nonlinearity, the forcing amplitude is increased to $\epsilon = 5 \times 10^{-2}$ and a wave packet is triggered close to the ogive-cylinder junction at $x = 9.46$ (Case 5). The wall pressure perturbation signature is shown in Fig. 17. Note that the amplitude scales have been adjusted in the subfigures to highlight the dominant features. Although the linear wave packets on the ogive-cylinders exhibit structures similar to those on the flat plates, the nonlinear behavior is clearly different. The signature of the initial disturbance development (Figs. 17(a-c)) is similar to the weak forcing case in Fig. 11(a-c). Circular arc-like waves constitute the leading front of the wave packet, followed by arrowhead-shaped structures in Fig. 17(a,b). At $x = 16$ (Fig. 17(c)), the dominance of $2D$ waves at the center of wave packet surrounded by azimuthally varying structures at the trailing end is evident.

Deviations from the weak forcing case become more pronounced further downstream. The azimuthal modulation of the wave fronts is noticeable in Fig. 17(d) and becomes more pronounced further downstream (Fig. 17(e)). The leading portion spreads over the span; however, the arrowhead structure with dominance of $2D$ waves is preserved. Disturbances spread further in the azimuthal direction, maintaining the three-legged structure of the wave packet (Fig. 17(f)). These structures could be attributed to the significant spanwise curvature in ogive-cylinder bodies, relative to the relevant instability wavelengths. In sharp cones, such structures were observed when forcing is imposed closer to the tip of the nose, but not for an actuation further downstream on the frustum [28]. This is not unanticipated because cones have a diverging shape downstream, and the spanwise curvature effects are more prominent closer to the nose than the base.

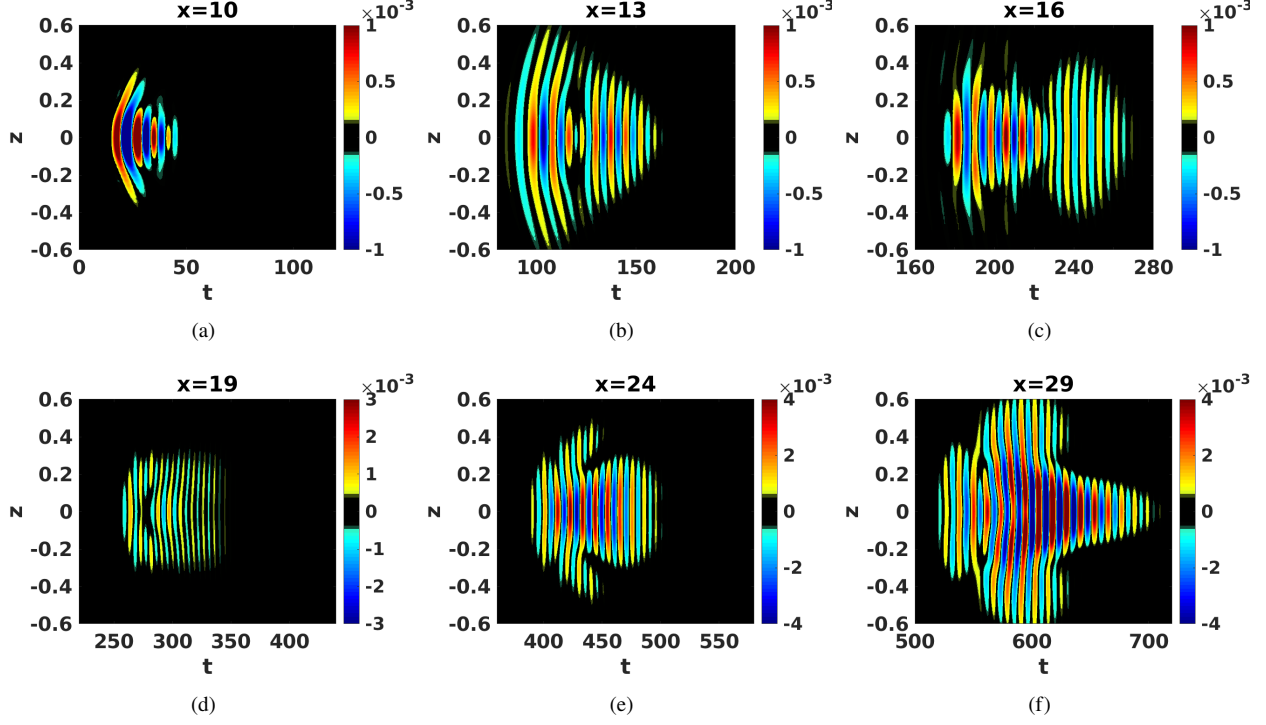


Fig. 17 Spatiotemporal evolution of wall pressure perturbations for nonlinear wave packet forcing (Case 5).

The spectral signature of the disturbance evolution (Fig. 18) further highlights the deviations from the linear wave packet. Stronger planar Mack modes ($f \sim 82 \text{ kHz}$) and weaker oblique first modes ($((f, \beta) = (22.6, \pm 10.19))$) are apparent in Fig. 18(a) i.e., the dominant $2D$ high-frequency and oblique lower-frequency waves features observed in the linear case (Fig. 12(b), Case 3) persist with nonlinear forcing. However, the larger amplitudes engender harmonics of the fundamental wave ($f \sim 141 \text{ kHz}$) due to the self-sum interaction, $(70.5, 0) + (70.5, 0) \rightarrow (141, 0)$. The energy is spread into spanwise waves, consistent with the pressure perturbations in Fig. 17(d). Proceeding downstream, the Mack mode and its harmonics are also observed for $x = 29$ (Fig. 18(c)), at lower frequencies than at upstream stations. The presence

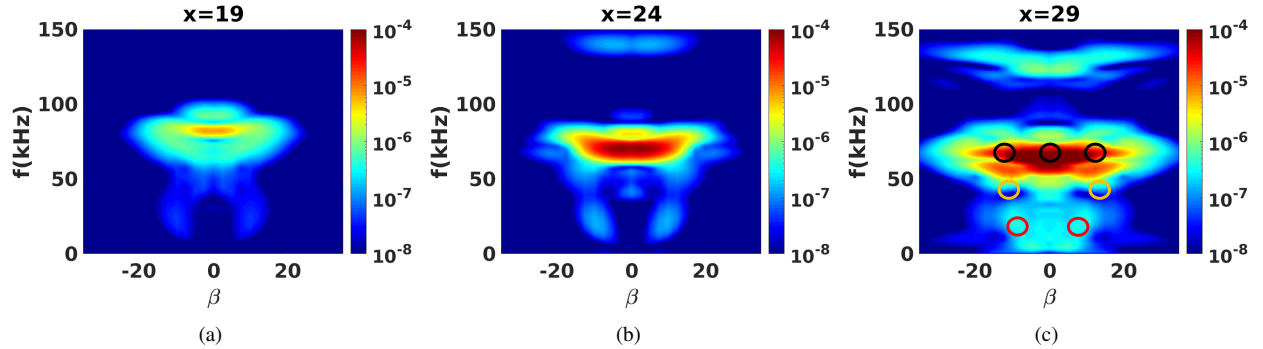


Fig. 18 Streamwise spectral evolution contours of nonlinear wave packet in the frequency (f) -spanwise wavenumber (β) plane (Case 5).

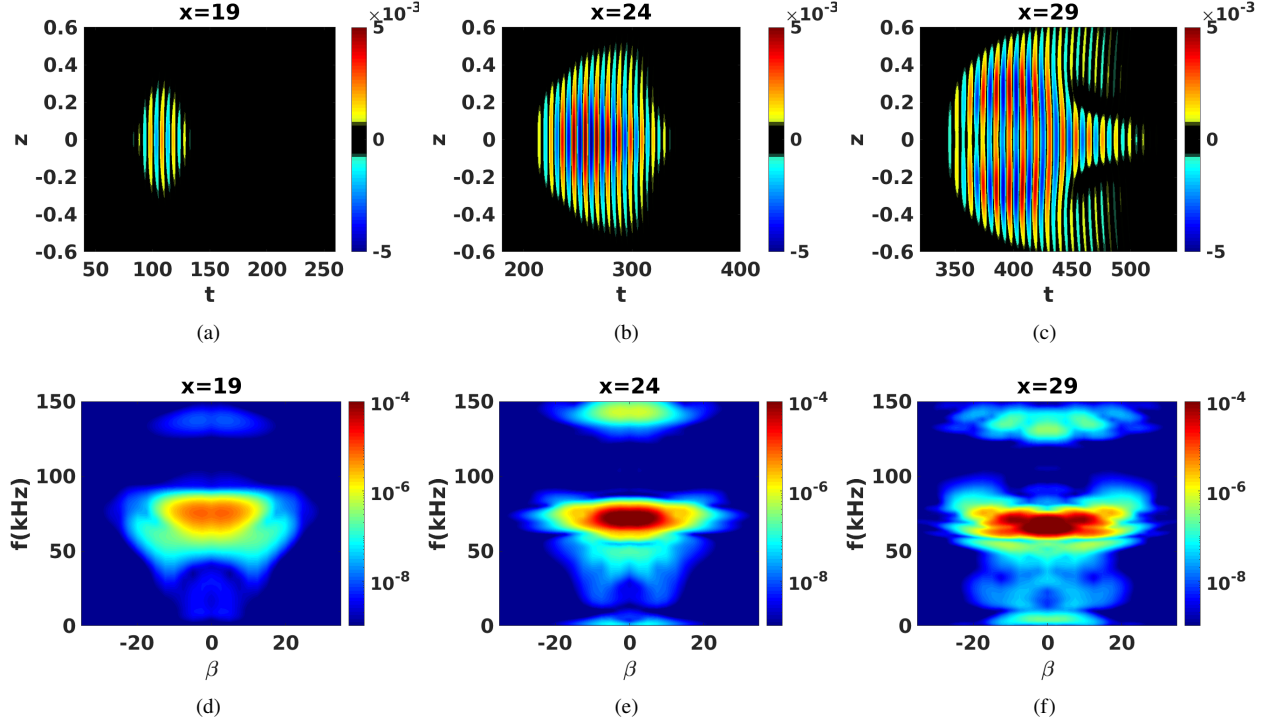


Fig. 19 Nonlinear wave packet evolution for disturbances triggered at $x = 16.2$ (Case 6). The wall pressure perturbation contours are shown in (a, b, c). The corresponding spectral content is plotted in (d, e, f).

of low-frequency disturbances indicate laminar mean flow distortion by the wave packet and deviations from the linear counterpart (Fig. 12(c)) also suggest the onset of secondary instabilities. Oblique waves at the same frequency as the second mode at $(f, \beta) = 65 \text{ kHz}, \pm 10$ exhibit large amplitudes. This further points to fundamental resonance [14] as a dominant secondary instability mechanism. Weak oblique disturbances at half the Mack mode frequency with $(f, \beta) = (32.5 \text{ kHz}, \pm 10)$ are also apparent, and can be interpreted as a signature of subharmonic resonance. While the above two secondary instabilities are related to the second mode, a third class of first-mode (weak) oblique resonance at $(f, \beta) = (20.6 \text{ kHz}, \pm 7.65)$ is also noted.

Case 6 examines effect of location of nonlinear wavepacket initiation on perturbation evaluation. The corresponding wall pressure perturbation and spectral signatures are shown in Fig. 19. An arrowhead-shaped wave packet is again observed in Fig. 19(a), similar to its linear counterpart (Fig. 13(a)) and a weaker oblique wave signature arises in the spectra (Fig. 19(d)). Additionally, higher amplitude forcing also manifests harmonics of the Mack modes. As it develops downstream (Fig. 19(b)), the pressure perturbation signature deviates from the linear wave packet, especially in the observation of a trailing edge protrusion and enhanced spanwise spreading. This is also reflected in its spectral signature (Fig. 19(e)) with oblique waves arising at the second-mode frequency. Other effects are the emergence of oblique first-mode waves and further lower-frequency disturbances. This difference from the low-amplitude case may be attributed to higher receptivity coefficients with higher-amplitude forcing. Hence, first-mode waves could be

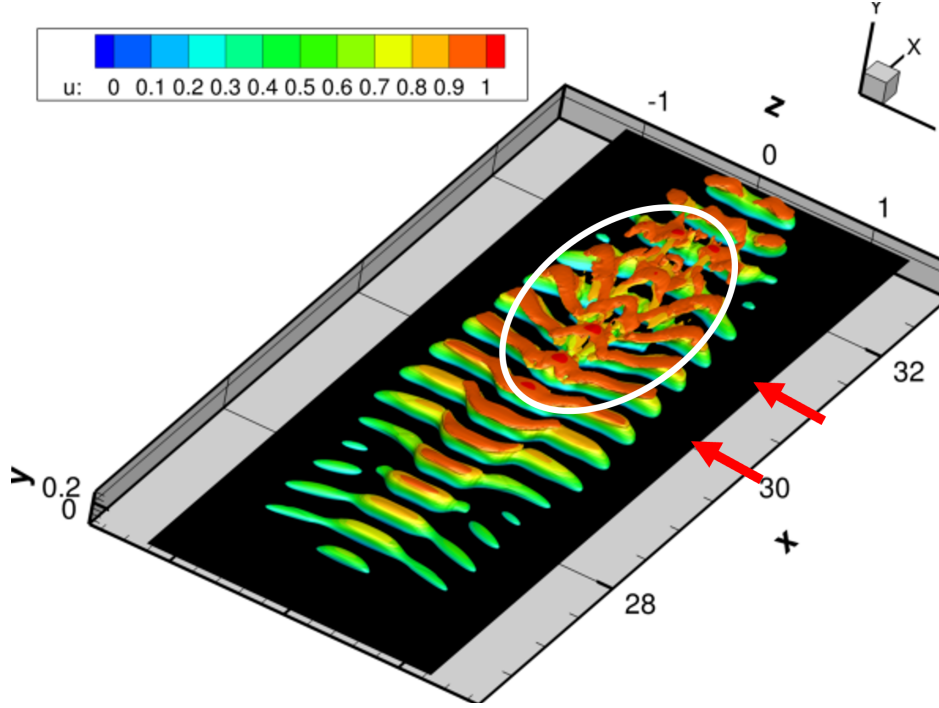


Fig. 20 Instantaneous vortical structures identified by Q-criterion ($Q = 0.2$) isosurfaces extracted at near the trailing end of the domain for Case 5.

triggered with a sufficiently strong disturbance source downstream of the ogive-cylinder junction. At $x = 29$ (Fig. 19(c)), the three-legged structure of the wave packet is evident, similar to Fig. 17(c). The spectral distribution suggests the dominance of the fundamental resonance with $(f, \beta) = (65.23, \pm 10)$. The evolution of the nonlinear wave packet with the two forcing locations considered suggests fundamental resonance as the dominant secondary instability mechanism.

The signature of vortical structures in the nonlinear regime for Case 5 is shown in Fig. 20. Similar to the linear wave packet, 2D roller structures are observed close to the wall. These are saturated because of the high forcing amplitudes, and develop a slightly oblique signature in the trailing part. The primary instabilities (Mack modes) after reaching sufficiently large amplitudes transfer their energies to secondary instabilities, which manifests as lambda vortices at $x = 30$ around $z = 0$. Further downstream ($x = 31$), these amplify by stretching in the streamwise direction along with some spanwise deformation. These lambda-patterns are (generally) aligned with each other, visually confirming the dominance of fundamental resonance.

The density gradient of the nonlinear wave packet (at $z = 0$) plotted in Fig. 21 also shows rope-like structures in $x \in [28, 30]$. These structures extend in the wall normal direction at $x = 31$ and resembling late transitional features reported by Hill et al. [3]. Their origin could be linked to the strong secondary instabilities observed at this location evident in Fig. 20.

The role of instabilities in generating the Schlieren signature can be explained through the density perturbation contours of the wave packet at various cross-flow planes, as shown in Fig. 22. At $x = 30$ (Fig. 22(a)), the density

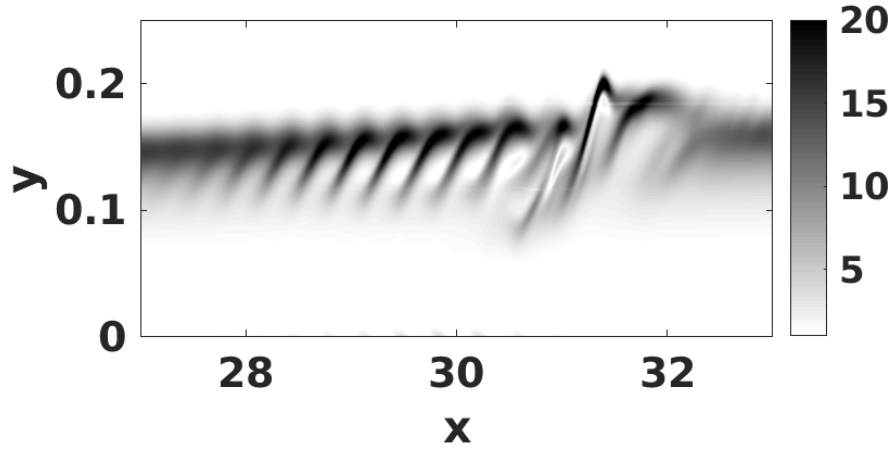


Fig. 21 Pseudo-Schlieren in the symmetry plane of instantaneous vortical structures (Case 5).

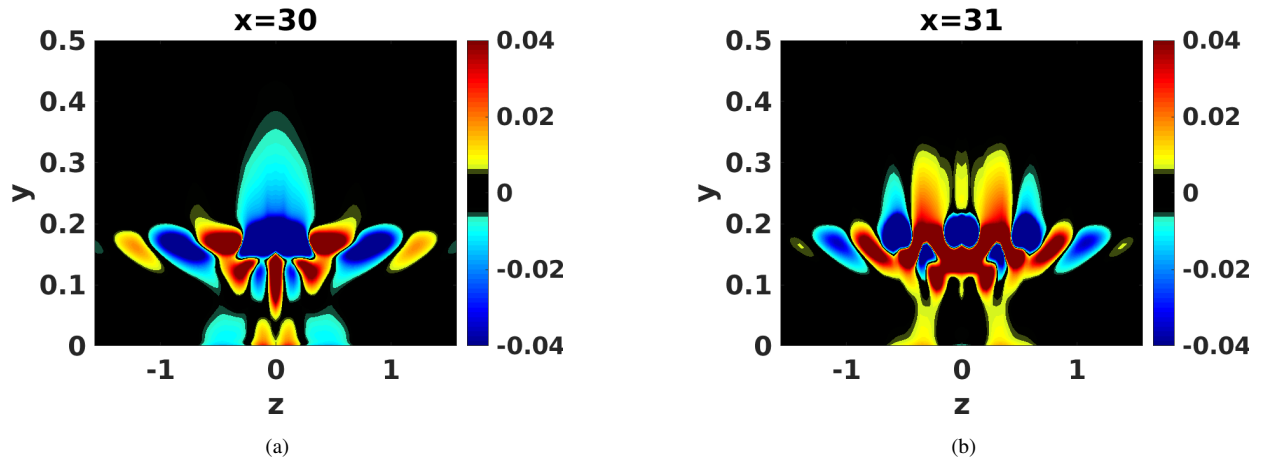


Fig. 22 Density perturbation contours in the cross-flow planes of instantaneous vortical structures (Case 5).

perturbation is strongest at locations away from the wall, $(y, z) \sim (0.2, 0)$ and is surrounded by oblique waves at $(y, z) \sim (0.2, -1)$ similar to the prior observations with the linear wave packet (Fig. 16). New smaller wavelength disturbances are observed in $(y, z) \sim (0.1, 0.2)$, suggesting deformation of the Mack mode. Spanwise spreading of the Mack modes is noticeable closer to the wall at $(y, z) \sim (0, 0)$. In Fig. 22(b) ($x = 31$), a significant deformation of the Mack mode structure is observed at $(y, z) \sim (0.2, 0)$, with a reduction in its spanwise extent and the development of new adjacent lambda-shaped structures. The wall-normal extension in the pseudo-Schlieren is due to these instabilities and can be considered to be the imprints of an energy transfer between primary and secondary instabilities. The resulting spanwise modulation signature is observed on the wall for $(y, z) \sim (0, \pm 0.5)$; however the waves at $(y, z) \sim (0.2, -1)$ do not significantly modulate the base flow.

IV. Conclusions

Linear and nonlinear disturbance evolution over the frustum of ogive-cylinders at Mach 6.1 are examined with high-fidelity numerical simulations to augment prior linear stability analyses. The geometry and freestream parameters are obtained from recent experiments conducted at the Air Force Research Laboratory Mach 6 wind tunnel. The linear response of the boundary layer to freestream stochastic pressure perturbations indicates that the most amplified frequencies closely match the experimental observations, and the evolution features of the intermittent wave packets are accurately captured. Planar Mack modes are identified as the dominant primary instabilities. Oblique first modes are also observed; these amplify over a relatively longer streamwise length but at an order of magnitude lower amplitude than Mack modes.

A more controlled scenario is examined by considering wave packet evolution. For this, a broadband wave packet centered around a second-mode wave frequency is excited at different locations on the ogive-cylinder. When the wave packet is initiated closer to the ogive-cylinder junction, an arrowhead-shaped wave packet evolves with a structure similar to those observed previously on hypersonic flat plates. The spectral content of these disturbances identify dominant second-mode and weaker first-mode instabilities. When the wave packet is introduced at a further downstream location, while the second-mode waves dominate the primary instabilities, the receptivity of the first-mode waves was found to be very low.

The nonlinear modulation of broadband disturbances is then examined through high-amplitude wave packet actuation. When the source of disturbances closer to the ogive-cylinder junction, the wave packet modulates in the azimuthal direction, forming three-legged structures due to the spanwise curvature effects. Spectral analysis shows strong fundamental resonance, followed by weak subharmonic and oblique resonances as secondary instability mechanisms. When the nonlinear wave packet is triggered further downstream, both first- and second-mode waves are observed. The three-legged structure of the wave packet is preserved, and fundamental resonance is the dominant secondary instability mechanism. Experimentally observed rope-like structures of Mack modes and their wall-normal deformation in late

transitional stages are captured in pseudo-Schlieren contours. These deformations are attributed to the onset of secondary instabilities over Mack modes closer to the edge of the boundary layer. In future work, the transition to turbulence through fundamental resonance of second modes will be examined to assess the differences from axisymmetric cones.

Acknowledgements

This research was supported by the Office of Naval Research (Grant: N00014-21-1-2408) monitored by Dr. E. Marineau with R. Burnes as the technical point of contact. Discussions with Dr. M. Choudhari, Dr. P. Paredes, and Prof. C. Hader are gratefully acknowledged. The opinions, findings, views, conclusions, or recommendations contained herein are those of the authors and should not be interpreted as necessarily representing the official policies or endorsements, either expressed or implied, of ONR or the U.S. Government. The simulations were carried out using resources provided by the U.S. Department of Defense High Performance Computing Modernization Program, Ohio Supercomputer Center, and FSU Research Computing Center.

References

- [1] Morkovin, M. V., “Transition at hypersonic speeds,” *27th Aerospace Sciences Meeting*, USA, 1987, p. 34.
- [2] Schneider, S. P., “Hypersonic laminar–turbulent transition on circular cones and scramjet forebodies,” *Progress in Aerospace Sciences*, Vol. 40, No. 1-2, 2004, pp. 1–50.
- [3] Luke Hill, J., Oddo, R. A., Komives, J. R., Reeder, M. F., Borg, M. P., and Jewell, J. S., “Experimental Measurements of Hypersonic Instabilities over Ogive-Cylinders at Mach 6,” *AIAA Journal*, 2022, pp. 1–17.
- [4] Huerre, P., and Monkewitz, P. A., “Local and global instabilities in spatially developing flows,” *Annual review of fluid mechanics*, Vol. 22, No. 1, 1990, pp. 473–537.
- [5] Novikov, A., Egorov, I., and Fedorov, A., “Direct numerical simulation of wave packets in hypersonic compression-corner flow,” *AIAA Journal*, Vol. 54, No. 7, 2016, pp. 2034–2050.
- [6] Reshotko, E., “Boundary-layer stability and transition,” *Annual review of fluid mechanics*, Vol. 8, No. 1, 1976, pp. 311–349.
- [7] Fedorov, A. V., and Khokhlov, A. P., “Prehistory of instability in a hypersonic boundary layer,” *Theoretical and Computational Fluid Dynamics*, Vol. 14, No. 6, 2001, pp. 359–375.
- [8] Saric, W. S., Reed, H. L., and Kerschen, E. J., “Boundary-layer receptivity to freestream disturbances,” *Annual review of fluid mechanics*, Vol. 34, No. 1, 2002, pp. 291–319.
- [9] Mack, L. M., “Boundary-layer linear stability theory,” Tech. rep., California Institute of Technology, Jet Propulsions Lab, Pasadena, 1984.

- [10] Masad, J. A., "Relationship between transition and modes of instability in high-speed boundary layers," *AIAA journal*, Vol. 33, No. 4, 1995, pp. 774–776.
- [11] Fedorov, A., and Tumin, A., "High-speed boundary-layer instability: old terminology and a new framework," *AIAA journal*, Vol. 49, No. 8, 2011, pp. 1647–1657.
- [12] Kendall, J. M., "Wind tunnel experiments relating to supersonic and hypersonic boundary-layer transition," *Aiaa Journal*, Vol. 13, No. 3, 1975, pp. 290–299.
- [13] Scholten, A., Paredes, P., Luke Hill, J., Borg, M., Jewell, J. S., and Choudhari, M. M., "Linear Instabilities over Ogive-Cylinder Models at Mach 6," *AIAA Journal*, 2022, pp. 1–14.
- [14] Herbert, T., "Secondary instability of boundary layers," *Annual review of fluid mechanics*, Vol. 20, No. 1, 1988, pp. 487–526.
- [15] Bushnell, D., "Notes on initial disturbance fields for the transition problem," *Instability and transition*, Springer, 1990, pp. 217–232.
- [16] Balakumar, P., and Chou, A., "Transition prediction in hypersonic boundary layers using receptivity and freestream spectra," *AIAA Journal*, Vol. 56, No. 1, 2018, pp. 193–208.
- [17] Marineau, E. C., Moraru, G. C., Lewis, D. R., Norris, J. D., Lafferty, J. F., and Johnson, H. B., "Investigation of Mach 10 boundary layer stability of sharp cones at angle-of-attack, part 1: experiments," *53rd AIAA Aerospace Sciences Meeting*, 2015, p. 1737.
- [18] Goparaju, H., Liu, Y., Duan, L., and Gaitonde, D. V., "Supersonic transition induced by numerical tunnel disturbances," *AIAA SCITECH 2022 Forum*, 2022, p. 1826.
- [19] Liu, Y., Schuabb, M., Duan, L., Paredes, P., and Choudhari, M. M., "Interaction of a Tunnel-like Acoustic Disturbance Field with a Blunt Cone Boundary Layer at Mach 8," *AIAA AVIATION 2022 Forum*, 2022, p. 3250.
- [20] Duan, L., Choudhari, M. M., Chou, A., Munoz, F., Radespiel, R., Schilden, T., Schröder, W., Marineau, E. C., Casper, K. M., Chaudhry, R. S., et al., "Characterization of freestream disturbances in conventional hypersonic wind tunnels," *Journal of Spacecraft and Rockets*, Vol. 56, No. 2, 2019, pp. 357–368. <https://doi.org/https://doi.org/10.2514/1.A34290>.
- [21] Hader, C., and Fasel, H. F., "Towards simulating natural transition in hypersonic boundary layers via random inflow disturbances," *Journal of Fluid Mechanics*, Vol. 847, 2018.
- [22] Goparaju, H., Unnikrishnan, S., and Gaitonde, D. V., "Effects of Nose Bluntness on Hypersonic Boundary-Layer Receptivity and Stability," *Journal of Spacecraft and Rockets*, 2021, pp. 1–17.
- [23] Fedorov, A., Ryzhov, A., Soudakov, V., and Utyuzhnikov, S., "Receptivity of a high-speed boundary layer to temperature spottiness," *Journal of Fluid Mechanics*, Vol. 722, 2013, pp. 533–553.

- [24] Ma, Y., and Zhong, X., "Receptivity of a supersonic boundary layer over a flat plate. Part 3. Effects of different types of free-stream disturbances," *Journal of Fluid Mechanics*, Vol. 532, 2005, pp. 63–109.
- [25] Cerminara, A., and Sandham, N. D., "Acoustic leading-edge receptivity for supersonic/hypersonic flows over a blunt wedge," *AIAA Journal*, Vol. 55, No. 12, 2017, pp. 4234–4244.
- [26] Fedorov, A. V., "Receptivity of a supersonic boundary layer to solid particulates," *Journal of Fluid Mechanics*, Vol. 737, 2013, pp. 105–131.
- [27] Chuvakhov, P. V., Fedorov, A. V., and Obraz, A. O., "Numerical modelling of supersonic boundary-layer receptivity to solid particulates," *Journal of Fluid Mechanics*, Vol. 859, 2019, pp. 949–971.
- [28] Hader, C., and Fasel, H. F., "Three-dimensional wave packets in a Mach 10 Boundary Layer on a Sharp Cone," *AIAA Aviation 2021 Forum*, 2021, p. 2943.
- [29] Sivasubramanian, J., and Fasel, H. F., "Numerical investigation of the development of three-dimensional wavepackets in a sharp cone boundary layer at Mach 6," *Journal of Fluid Mechanics*, Vol. 756, 2014, pp. 600–649.
- [30] Casper, K. M., Beresh, S. J., and Schneider, S. P., "Pressure fluctuations beneath instability wavepackets and turbulent spots in a hypersonic boundary layer," *Journal of Fluid Mechanics*, Vol. 756, 2014, pp. 1058–1091.
- [31] Sivasubramanian, J., Tumin, A., and Fasel, H. F., "The Reynolds number effect on receptivity to a localized disturbance in a hypersonic boundary layer," *8th AIAA Flow Control Conference*, 2016, p. 4246.
- [32] Unnikrishnan, S., and Gaitonde, D. V., "Linear, nonlinear and transitional regimes of second-mode instability," *Journal of Fluid Mechanics*, Vol. 905, 2020.
- [33] Sandberg, R. D., "Governing equations for a new compressible Navier-Stokes solver in general cylindrical coordinates," 2007.
- [34] Jameson, A., Schmidt, W., and Turkel, E., "Numerical solution of the Euler equations by finite volume methods using Runge Kutta time stepping schemes," *14th fluid and plasma dynamics conference*, 1981, p. 1259.
- [35] Beam, R. M., and Warming, R., "An implicit factored scheme for the compressible Navier-Stokes equations," *AIAA journal*, Vol. 16, No. 4, 1978, pp. 393–402.
- [36] Balsara, D. S., and Shu, C.-W., "Monotonicity preserving weighted essentially non-oscillatory schemes with increasingly high order of accuracy," *Journal of Computational Physics*, Vol. 160, No. 2, 2000, pp. 405–452.
- [37] Roe, P. L., "Approximate Riemann solvers, parameter vectors, and difference schemes," *Journal of computational physics*, Vol. 43, No. 2, 1981, pp. 357–372.
- [38] Visbal, M. R., and Gaitonde, D. V., "On the use of higher-order finite-difference schemes on curvilinear and deforming meshes," *Journal of Computational Physics*, Vol. 181, No. 1, 2002, pp. 155–185.

- [39] Gupta, R., Lee, K., Zoby, E., Moss, J., and Thompson, R., “Hypersonic viscous shock-layer solutions over long slender bodies. I-High Reynolds number flows,” *Journal of Spacecraft and Rockets*, Vol. 27, No. 2, 1990, pp. 175–184.
- [40] Scholten, A., Paredes, P., Hill, J. L., Borg, M. P., Jewell, J. S., and Choudhari, M. M., “Hypersonic Boundary-Layer Instabilities over Ogive-Cylinder Models,” *AIAA SCITECH 2022 Forum*, 2022, p. 1579.
- [41] Kennedy, R. E., Jagde, E. K., Laurence, S. J., Jewell, J. S., and Kimmel, R. L., “Visualizations of Hypersonic Boundary-Layer Transition on a Variable Bluntness Cone,” *AIAA Aviation 2019 Forum*, 2019, p. 3079.
- [42] Schmid, P. J., “Dynamic mode decomposition of numerical and experimental data,” *Journal of fluid mechanics*, Vol. 656, 2010, pp. 5–28.
- [43] Chen, K. K., Tu, J. H., and Rowley, C. W., “Variants of dynamic mode decomposition: boundary condition, Koopman, and Fourier analyses,” *Journal of nonlinear science*, Vol. 22, No. 6, 2012, pp. 887–915.
- [44] Sivasubramanian, J., and Fasel, H., “Transition initiated by a localized disturbance in a hypersonic flat-plate boundary layer,” *49th AIAA Aerospace Sciences Meeting including the New Horizons Forum and Aerospace Exposition*, 2011, p. 374.
- [45] Sivasubramanian, J., and Fasel, H. F., “Direct numerical simulation of transition in a sharp cone boundary layer at Mach 6: fundamental breakdown,” *Journal of Fluid Mechanics*, Vol. 768, 2015, pp. 175–218.
- [46] Marineau, E. C., Grossir, G., Wagner, A., Leinemann, M., Radespiel, R., Tanno, H., Chynoweth, B. C., Schneider, S. P., Wagnild, R. M., and Casper, K. M., “Analysis of Second-Mode Amplitudes on Sharp Cones in Hypersonic Wind Tunnels,” *Journal of Spacecraft and Rockets*, Vol. 56, No. 2, 2019, pp. 307–318. <https://doi.org/https://doi.org/10.2514/1.A34286>.
- [47] Browne, O. M., Al Hasnine, S. M., and Brehm, C., “Numerical Method for Particulate-Induced High-Speed Boundary-Layer Transition Simulations,” *AIAA Journal*, Vol. 59, No. 4, 2021, pp. 1196–1213.
- [48] Goparaju, H., and Gaitonde, D. V., “Role of entropic-instabilities in laminar-turbulent transition on a blunted flat plate,” *arXiv preprint arXiv:2112.10049*, 2021.
- [49] Scholten, A., Goparaju, H., Gaitonde, D. V., Paredes, P., Choudhari, M. M., and Li, F., “Linear Disturbance Amplification Over Blunted Flat Plates in High-Speed Flows,” *AIAA AVIATION 2022 Forum*, 2022, p. 3471.
- [50] Hunt, J. C., Wray, A. A., and Moin, P., “Eddies, streams, and convergence zones in turbulent flows,” *Studying turbulence using numerical simulation databases, 2. Proceedings of the 1988 summer program*, 1988.
- [51] Lees, L., and Lin, C. C., “Investigation of the stability of the laminar boundary layer,” *NASA Tech Reports*, 1946, pp. 69–87.